2014 13th International Conference on Control, Automation, Robotics & Vision
Marina Bay Sands, Singapore, 10-12th December 2014 (ICARCV 2014)

A New Statistical and Dirichlet Integral Framework Applied to Liver Segmentation from Volumetric CT Images

Changyang Li, Ang Li, Xiuying Wang, Dagan Feng
Biomedical and Multimedia Information Technology (BMIT) Research Group, School of IT, the University of Sydney, Australia
[changyang.li; ang.li; xiu.wang; dagan.feng]@sydney.edu.au

Stefan Eberl, Michael Fulham
Department of PET and Nuclear Medicine, Royal Prince Alfred Hospital, Sydney, Australia
Sydney Medical School, University of Sydney,
stefan.eberl@sydney.edu.au; michael.fulham@sydney.edu.au

***Abstract*—Accurate liver segmentation from computed tomography (CT) images is problematic due to non-uniform density, weak boundaries and because there may be multiple liver tumors that have heterogeneous intensities in region(s) of interest (ROIs). So we propose a generalized energy framework that harnesses the statistical intensity approximation with image data on graphs. Our statistical energy term takes advantage of the mixture-of-mixtures Gaussian model to approximate the probability density distribution of the liver and background to better differentiate between the two. The probability density estimation can be combined with the spatial cohesion of the graph-based Dirichlet integral by using graph calculus. Matrix decomposition and differentiation are used to minimize our proposed energy functional. We tested our approach on 20 public high-contrast CT images with single and multiple liver tumors. Our method had an average dice similarity coefficient (DSC) of 93.75±1.29%, an average false positive (FP) rate of 9.43±3.52% and an average false negative (FN) rate of 3.48±1.48%. Our method outperformed the benchmark graph-based Random Walker algorithm (average DSC=81.97±4.09%, average FP rate 34.10±10.53%, and average FN rate 7.10±4.35%).**

***Keywords*—Image segmentation, mixture-of-mixtures Gaussian, Dirichlet integral, energy miminization**

I. INTRODUCTION

The liver is commonly involved in metastatic disease and in the past such involvement often meant that the underlying disease was not treatable. Improvements in surgical and interventional radiology techniques and chemotherapy, however, now offer opportunities for effective palliation and prolonged disease free survival. Such local hepatic therapies require accurate liver segmentation as a fundamental step in treatment planning. Although computer aided techniques for segmentation are available, there is still heavy reliance on manual techniques which are time-consuming, operator intensive and poorly reproducible.

For further background, early hepatic segmentation approaches used intensity estimation, morphologic operators, and the deformable contour model. More recently, voxel classification / clustering [1, 2], level set methods [3-5] and graph-based segmentation algorithms [6, 7] have been reported by a number of investigators. The voxel classification / clustering approaches calculate the probability density of each voxel by using different statistical models, e.g. fuzzy C-means and finite Gaussian distributions, to estimate the intensity distribution of regions of interest (ROIs.) Unsupervised classification is performed on the input image to acquire a statistical characterization without any prior probability estimations. These models often use iterative schemes, such as the expectation maximization (EM) algorithm [8], to optimize the multiple parameters for better probability density approximation. Unsupervised classifiers are subject to disjointed segmentation results that lack spatial cohesion. Supervised classifiers often develop statistical shape modelling [9] or probabilistic atlases [10] to provide prior probability estimations of the target and spatial cohesion. The liver, however, varies in shape and volume, in particular, when it is infiltrated with multiple metastatic tumors of varying sizes, and so it is difficult to obtain adequate training datasets and annotations for supervised classifiers.

Level set methods also minimize an objective energy formulation derived from image data and are widely used in medical image segmentation. Region-based level set methods utilize region statistical estimations to avoid the gradient detection that is a major issue in gradient-based energy models and they improve the robustness of image segmentation in the presence of image noise and weak boundaries [11]. Similar to priors in supervised classifiers, shape variations can be incorporated with energy formulation to influence the contour evolution with the global information of the expected shape. Wimmer et al. [12] combined shape priors with a region- and gradient-based energy formulation under a unified level set representation to segment liver CT images. However, level set methods are easily trapped in local minima and another major limitation is the requirement to specify multiple free parameters to balance energy weights in the energy functional [7].

Graph-based segmentation algorithms formulate an image as a graph, which consists of a lattice of vertices and edges connecting the vertices. The objective graph functional is minimized to obtain the segmentation. Variations of these algorithms originate from graph-cut (GC) [13], the random walker algorithm (RW) [7] and shortest paths [14]. The RW

978-1-4799-5199-4/14/$31.00 ©2014 IEEE

offers a confidence value for each voxel (pixel) belonging to each segment and hence produces better image segmentation than the GC [7]. The robustness and accuracy of the RW, however, are still limited by locations of seeds since variations in the boundary conditions (locations of seeds) result in different harmonic functions [15]. In addition, the RW may fail to segment an object with blurred and indistinct boundaries, which are often found in liver ROIs.

In this paper, we propose a new generalized energy framework model that accounts for probability density estimation and global spatial graph-based properties. A mixture of a multivariate Gaussian model solves the problem of non-uniform density and provides probability density estimations for foreground and background based on region intensity distributions when compared to the graph-based Dirichlet Integral energy functional. The probability density approximation on graphs is considered as region statistical inference and is incorporated with a graph-based Dirichlet Integral energy functional to overcome the limitation of boundary conditions with the RW.

II. STATISTIAL AND DIRICHLET INTEGRAL FRAMEWORK

The liver varies in shape and size across patients. In the abdomen, the different viscera (liver, bowel, kidneys, and spleen) and also intercostal chest wall muscles have overlapping intensity ranges and so isolated density estimations are unsuitable for separating the different organs. In this paper, we consider probability density estimation as region statistical inference. Accordingly, we use a combinatorial graph modeling to formulate statistical and Dirichlet Integral (SDI) energy functional for user-specific target segmentation and to provide a stable solution for liver segmentation in CT images.

We firstly define the general expression of a generalized energy functional to determine the label of every node as follows:

$$E = \lambda E_{mp} + E_{rw} \tag{1}$$

where E_{mp} is the statistical term that requires the function to better approximate the intensity distribution; and E_{rw} is the image data constraint to assign the label by using Dirichlet Integral to model image data.

We followed the graph definition of the RW to define E_{rw}. Let Ω be the image domain; $u:\Omega \to \Re$ be a gray level image that consists of N voxels. A graph G consists of a pair $G=(V,E)$ with node $\upsilon \in V$ and edge $e \in E \subseteq V \times V$. In image domain, a node υ_i would be simplified as a node/voxel i in a given image. The discrete version of the weighted Dirichlet integral is formulated to solve the calculation of the voxel's memberships [7]:

$$E_{rw} = \frac{1}{2} x^T L x = \frac{1}{2} \sum_{e_{ij} \in E} w_{ij} \left(x_i - x_j \right)^2 \tag{2}$$

where x is a vector containing the confidence values belonging to defined segments for all the image voxels, and L is the combinatorial Laplacian matrix and its element is given as:

$$L = \begin{cases} d_i & \text{if } i = j \\ -w_{ij} & \text{if nodes } v_i \text{ and } v_j \text{ are adjacent} \\ 0 & \text{otherwise} \end{cases} \tag{3}$$

where $d_i = \sum_j w_{ij}$ is the degree of a voxel i, which is defined as the sum of all weights of edges connecting to a voxel i; and w_{ij} is an edge weight between the voxel i and the neighboring voxel j:

$$w_{ij} = \exp\left(-\beta \left(g_i - g_j \right)^2 \right) \tag{4}$$

where β is the free weight parameter; g_i is the image gray value at voxel i, and $\left(g_i - g_j \right)^2$ is normalized to $[0, 1]$. The edge weight w_{ij} represents the likelihood that a random walker would cross the edge.

In abdominal CT, the intensity histograms of liver and background ROIs have multiple distinct peaks, which follow the assumption of the mixture-of-mixtures Gaussian model (MMGM) [16], where each component consists of a parametric mixture. However, MMGM only takes the intensity information into account and potentially misclassifies pixels with the same Gaussian mode, but belonging to different regions, into the wrong class in the image segmentation problem. Hence, we embed spatial cohesion of the graph paths with MMGM to determine the membership of each pixel. For this paper, we assume that the value of each voxel is drawn independently from intensity distributions. Accordingly, we modeled probability density descriptors by using the MMGM to represent the multimodal intensity distribution of the liver (foreground) and the background for each voxel in a given image:

$$p\left(i \mid \Theta \right) = \sum_{\eta=1}^{K} \pi_\eta p_\eta(i) = \sum_{\eta=1}^{K} \pi_\eta \left(\sum_{\alpha=1}^{M_{modes}} c_\alpha^\eta G_\alpha^\eta \left(g\left(i \right) \right) \right) \tag{5}$$

where Θ is the full set of Gaussian parameters and $G_\alpha^\eta \left(g\left(i \right) \mid \mu_\alpha^\eta, \sigma_\alpha^\eta \right)$ denotes a probability density in term of a finite Gaussian component by using mean μ_α^η and standard deviation σ_α^η; K is the number of segments (liver and background in our application) and M_{modes} is number of Gaussian components, which was set $M_{modes} = 2$ when $\eta = 1$ (foreground) and $M_{modes} = 4$ when $\eta = 2$ (background); π_η and c_α^η are the mixing coefficients of the segments and the modes.

We can assume each label is equally likely for both foreground and background by assigning $\pi_\eta = 0.5$. Then, we can normalize and define a probability density estimation calculus as below:

$$x_i^k = \frac{p_k(i)}{\sum_{\eta=1}^{K} p_\eta(i)} \tag{6}$$

where $p_\eta(i) = \sum_{\alpha=1}^{M_{modes}} c_\alpha^\eta G_\alpha^\eta\left(g(i)\right)$.

We can intuitively define a fitting constraint functional to penalize the function to be close to the probability density estimation as follows:

$$E_{mp\_voxel}(x_i) = \sum_{i=1}^{N}\sum_{k=1}^{K}\left(x_i^k \sum_{\eta=1}^{K} p_\eta(i) - p_k(i)\right)^2 \tag{7}$$

To define the probability density estimation (5) on graphs and maintain (6) as the solution of minimization energy, we use a diagonal matrix Λ, which is inspired by Grady [17], to represent $\sum_{\eta=1}^{K} p_\eta(i)$. (7) is written in vector notation as:

$$E_{mp}(x) = \left(\sum_{\eta=1}^{K}\Lambda^\eta\right)^{-1}\left(\left(\sum_{\eta=1}^{K}\Lambda^\eta\right)x - P\right)^T\left(\left(\sum_{\eta=1}^{K}\Lambda^\eta\right)x - P\right) \tag{8}$$

where P is a vector containing the probability density estimation values belonging to each segment (the total is K) for all the image voxels.

By combining (2) with (8), we provide a complete functional for (1) as:

$$E(x) = \frac{1}{2}x^T Lx + \lambda\left(\sum_{\eta=1}^{K}\Lambda^\eta\right)^{-1}\left(\left(\sum_{\eta=1}^{K}\Lambda^\eta\right)x - P\right)^T\left(\left(\sum_{\eta=1}^{K}\Lambda^\eta\right)x - P\right) \tag{9}$$

In (9), there are two potential minimization solutions in terms of different initializations. We provide the minimization solution with the input of labeled voxels to incorporate spatial cohesion in this paper. Accordingly, the nodes can be partitioned into two sets: the labeled set V_M and the unlabeled set V_U. Intuitively, we have $V_M \bigcup V_U = V$ and $V_M \bigcap V_U = \varnothing$. We can decompose the probability matrix $x = \begin{bmatrix} x_M \\ x_U \end{bmatrix}$ and $L = \begin{bmatrix} L_M & B \\ B^T & L_U \end{bmatrix}$ where x_M and x_U are labeled and unlabeled nodes; L_M, B, B^T, and L_U are constituents of the partitioned matrix decomposed from L. Thereby, (9) can be formulated as:

$$E(x_U) = \frac{1}{2}\begin{bmatrix} x_M^T x_U^T \end{bmatrix}\begin{bmatrix} L_M & B \\ B^T & L_U \end{bmatrix}\begin{bmatrix} x_M \\ x_U \end{bmatrix} + \lambda\left(\sum_{\eta=1}^{K}\Lambda^\eta\right)^{-1}\left(\left(\sum_{\eta=1}^{K}\Lambda_U^\eta\right)x_U - P_U\right)^T\left(\left(\sum_{\eta=1}^{K}\Lambda_U^\eta\right)x_U - P_U\right) \tag{10}$$

To solve the energy minimization of (10), we differentiate $E(x_U)$ with respect to x_U and find the critical point as:

$$x_U = \left(L_U + \lambda\sum_{\eta=1}^{K}\Lambda_U^\eta\right)^{-1}\left(\lambda P_U - B^T x_M\right) \tag{11}$$

Note that the fitting constraint contains the probability density estimation for all the voxels; and the trade-off between the fitting constraint E_{mp} and the image data E_{rw} is captured by a positive parameter λ.

We used the EM algorithm to optimize the MMGM parameters for the vector P estimation in (11). We provided an optimization solution for probability density estimation $p(i|\Theta)$ as follows. We used K-means to initialize the mean μ_α^η and standard deviation σ_α^η and then the EM procedures are given for (5):

1. E step: Evaluate the responsibilities $\gamma_\alpha(i)$ using the current parameters values

$$\gamma_\alpha(i) = \frac{N\left(g(i)C(i)\,|\,\mu_\alpha^\eta, \sigma_\alpha^\eta\right)}{\sum_{k=1}^{M_{modes}} N\left(g(i)C(i)\,|\,\mu_k^\eta, \sigma_k^\eta\right)} \tag{12}$$

where $C(i)$ denotes the pre-defined voxel samples for foreground and background.

2. M step:

$$\begin{cases} \left(\mu_\alpha^\eta\right)^{new} = N_\eta^{-1}\sum_{i=1}^{N}\gamma_\alpha^\eta(i)g(i)C(i) \\ \left(\left(\sigma_\alpha^\eta\right)^2\right)^{new} = N_\eta^{-1}\sum_{i=1}^{N}\gamma_\alpha^\eta(i)\left(g(i) - \left(\mu_\alpha^\eta\right)^{new}\right)^2 C(i) \\ \left(c_\alpha^\eta\right)^{new} = \left(\sum_{i=1}^{N} C(i)\right)^{-1} N_\eta \end{cases} \tag{13}$$

where $N_\eta = \sum_{i=1}^{N}\gamma_\alpha^\eta(i)C(i)$.

3. Evaluate the log likelihood:

$$\sum_{i=1}^{C(i)} \ln p\left(i\,|\,c_\alpha^\eta, \mu_\alpha^\eta, \sigma_\alpha^\eta\right) = \sum_{i=1}^{C(i)} \ln\left\{\left(\sum_{\alpha=1}^{M_{modes}} c_\alpha^\eta G_\alpha^\eta\left(g(i)\,|\,\mu_\alpha^\eta, \sigma_\alpha^\eta\right)\right)\right. \tag{14}$$

where $\Phi=\{c_\alpha^\eta, \mu_\alpha^\eta, \sigma_\alpha^\eta\}$

In the following section, we used the liver segmentation application to evaluate the performance of (11).

III. Experimental Results and Evaluation

A. Data Description

We used a publicly accessible dataset, which comprises 20 studies from the 3D Image Reconstruction for Comparison of Algorithm Database (3D-ICRADb) [18], to evaluate the algorithms. This dataset includes anonymized venous phase CT images of 10 male and 10 female patients, who were scanned in a variety of European hospitals with different CT scanners. The image size of this dataset is 512×512 and pixel sizes vary from 0.56 to 0.87 mm. Inter-slice distances range from 1.0 to 2.5mm. Corresponding manual segmentation images of structures of interest (such as liver, heart, pancreas, etc.) in DICOM format were also provided by clinical experts. The manually segmented liver contours were used as the ground truth to evaluate the accuracy of our proposed segmentation algorithm.

B. Measurement

We used the Dice Similarity Coefficient (DSC) to evaluate the accuracy of the results. The DSC is defined as:

$$DSC(V_s, V_m) = 2\left|V_s \cap V_m\right| / \left(\left|V\right|_s + \left|V_m\right|\right) \times 100\% \qquad (15)$$

where V_s is the segmentation result and V_m denotes the ground-truth volume. A DSC of 100% indicates complete agreement with the ground truth; whereas DSC = 0% indicates that the segmentation result does not overlap the ground-truth at all.

We also evaluated segmentation results using false positive (FP) and false negative (FN) rates, which are measurements of over-segmentation and under-segmentation and are defined below:

$$FPR(V_s, V_m) = (V_s - (V_s \cap V_m)) / V_m \times 100\% \qquad (16)$$

$$FNR(V_s, V_m) = (V_m - (V_s \cap V_m)) / V_m \times 100\% \qquad (17)$$

C. Initialization and implementation

We used the same $\beta = 90$ for both SDI and RW; and the parameter $\lambda = 2e-3$ in (11) was determined empirically for our SDI in all the experiments. In the SDI, the MMGM was used to approximate the intensity distribution of liver and background. Since the liver contains normal and tumor tissue, we used 2 for the foreground modes and 4 for the background modes.

The SDI and the RW are seeded segmentation algorithms. Since segmentation results may vary from different seed inputs, we provided the same seed initialization for SDI and the RW, which is a typical experimental comparison for seeded image segmentation algorithms [15, 19, 20]. Our aim was to evaluate performance and produce a quantitative, reproducible evaluation. Foreground seeds were selected by using centroid of the ground truth and expanding it to the edge with a width of 2 voxels. Background seeds were selected through dilation of the target regions with a disk structure element of 35 voxels. Foreground and background seeds are represented by blue and green contours, respectively, in Figure 3.

The implementation of our proposed method was performed on an Intel 2.40 GHz Quad Core PC with 8GB RAM and a single thread, and the average processing time for one image volume was approximately 9 minutes.

D. Segmentation results evaluation

The averages and standard deviations of DSC, FP and FN volume measurements are summarized in TABLE I. We found that our algorithm improved the accuracy of liver segmentation when compared to the RW based on the DSC. Our proposed SDI achieved lower average FP and FN rates indicating that our algorithm was less prone to over-segmentation and under-segmentation in liver segmentation than the RW.

TABLE I. DSC, FP and FN (Mean ± Standard) Results for SDI and the RW

Model	Measurements		
	DSC	*FP*	*FN*
SDI	93.75 ±1.29%.	9.43% ± 3.52%	3.48% ± 1.48%
RW	81.97 ± 4.09%	34.10% ± 10.53%	7.10% ± 4.35%

The comparison of the two segmentation algorithms for the 20 datasets is shown in Figure 1, where each pair of the bars shows the DSC of our proposed SDI (yellow) and the RW (blue). The FP and FN rates of the two algorithms for all the testing datasets are illustrated in Figure 2. Our evaluation indicates that erroneous segmentations in both algorithms are mainly attributed to over-segmentation, and that our algorithm obtained lower error rates of over- and under-segmentation.

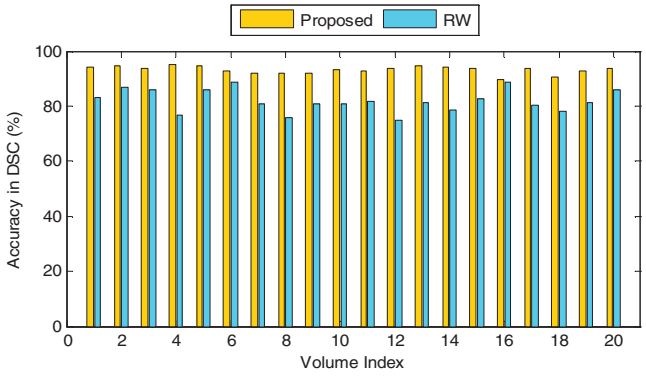

Figure 1 A quantitative evaluation on DSC accuracy of our SDI and RW on a cohort of 20 liver CT volumes.

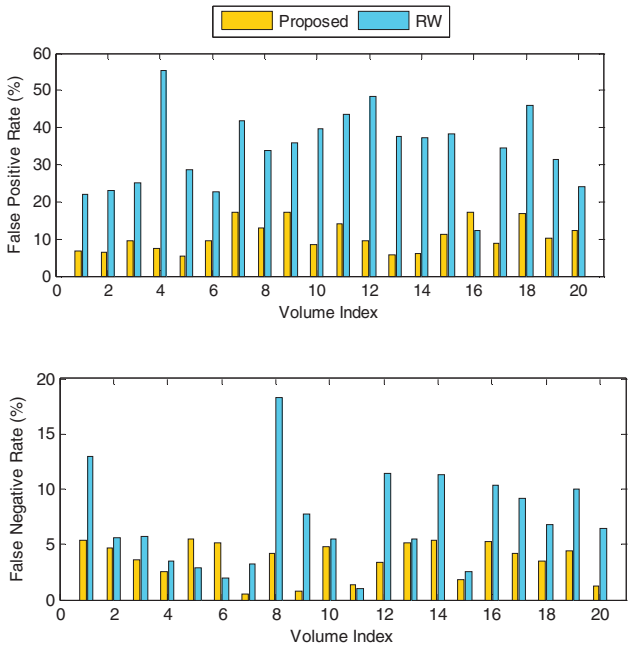

Figure 2 A quantitative evaluation on false positive (top) and negative (bottom) rates of our proposed SDI and RW.

Four different representative groups of CT liver segmentation examples were chosen to qualitatively compare our proposed algorithm with the RW in Figure 3. In Figure 3, row 1 shows a transaxial CT image where the liver lies adjacent to the stomach and just below the heart with the bases of the lungs shown on both sides; row 2 shows the liver as the dominant structure in the upper abdomen with the fundus of the stomach adjacent to it and the spleen in the left upper quadrant with the base of the lung fields shown once again, posteriorly; row 3 shows a lower slice of the liver adjacent to loops of bowel and the right kidney, which have similar intensity ranges; row 4, is at the level of the mid-portion of the liver which has multiple tumors that display spurious gradients and different intensities; loops of bowel lie adjacent to the liver and the spleen is seen in the left side of the upper abdomen. As seen in Figure 3, the RW can be prone to leakage into adjacent structures (rows 3 and 4 where there is leakage into adjacent muscle and soft tissue of the lateral abdominal wall) and under segmentation (row 2) where the RW misses the entire edge of the left lobe of the liver. For the RW the FP rate reflects the over segmentation (leakage) and the FN rate, the under segmentation, as seen in Figure 3. In contrast, the SDI method shows little leakage into adjacent structures (see Figure 3 rows 2 and 3 where there is no leakage into the stomach and bowel which are immediately adjacent to the liver) and there is not any pronounced under-segmentation, which attests to the higher accuracy and robustness of the SDI algorithm when compared to the RW.

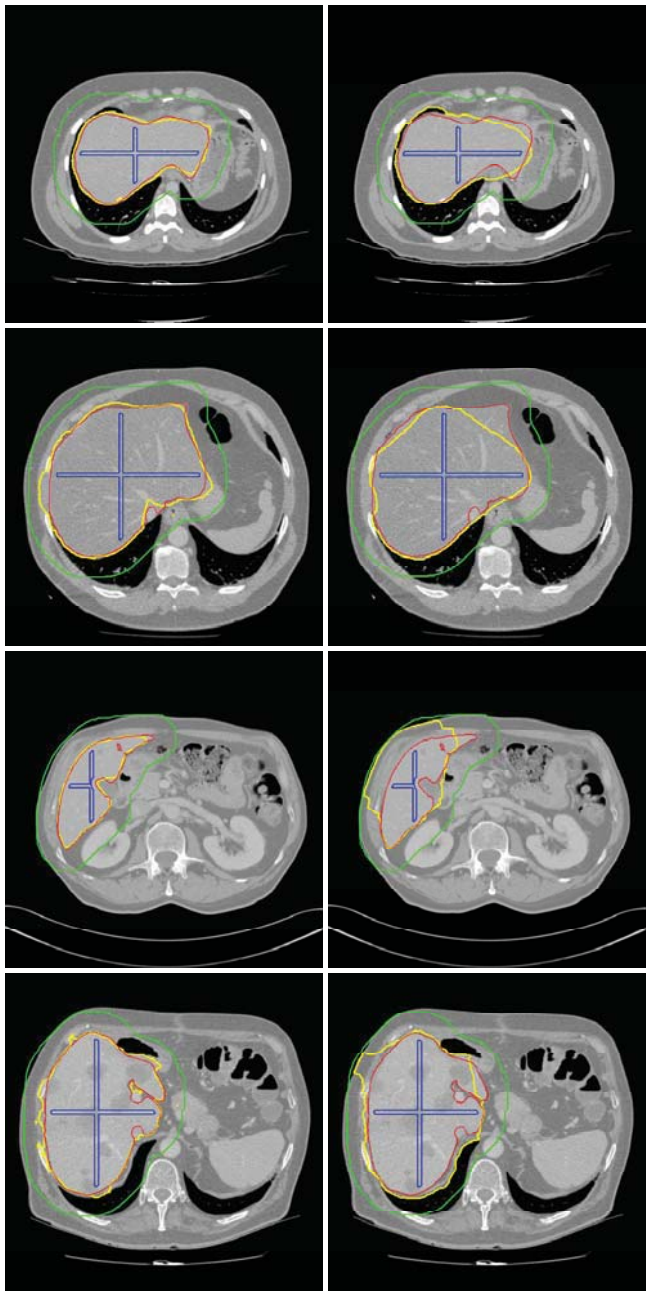

Figure 3 Examples of 4 different segmentation results from 4 test cases (1st row: case Volume 2, 2nd row: case Volume 16, 3rd row: case Volume 4 and 4th row: case Volume 6) using (a) our SDI (1st column) and (b) the RW (2nd column). (Blue contour = foreground seeds; green contour = background seeds; red contour = ground truth; and yellow contour = segmentation result)

IV. Conclusion

We propose a generalized statistical and Dirichlet integral framework to embed the statistical approximation on graphs and applied it to segmentation of liver CT images. We provided a complex statistical model- MMGM on graphs representation and used derived probability density estimations to better classify voxels with overlapping intensity ranges, which often result in blurred boundaries in CT images. We used

combinatorial analogues of standard operators and differentiation to solve our proposed generalized energy functional. Comparative experimental liver segmentation results from 20 abdominal CT volumes show that our algorithm is more robust and accurate that the RW.

REFERENCES

[1] G. Tian, Y. Xia, *et al.*, "Hybrid Genetic and Variational Expectation-Maximization Algorithm for Gaussian-Mixture-Model-Based Brain MR Image Segmentation," *IEEE Trans. Inf. Technol. Biomed.,* vol. 15, pp. 373-380, 2011.

[2] X. Liu, M. G. Linguraru, *et al.*, "Organ pose distribution model and an MAP framework for automated abdominal multi-organ localization," in *Proc. of 5th Intl. Conf. on MIAR*, Beijing, China, 2010, pp. 393-402.

[3] C. Li, X. Wang, *et al.*, "A New Energy Framework With Distribution Descriptors for Image Segmentation," *IEEE Trans. Image Process.,* vol. 22, pp. 3578-3590, 2013.

[4] S. Lankton and A. Tannenbaum, "Localizing Region-Based Active Contours," *IEEE Trans. Image Process.,* vol. 17, pp. 2029-2039, 2008.

[5] C. Li, X. Wang, *et al.*, "A Likelihood and Local Constraint Level Set Model for Liver Tumor Segmentation from CT Volumes," *IEEE Trans. Biomed. Eng.,* vol. 60, pp. 2967-2977, 2013.

[6] L. Massoptier and S. Casciaro, "Fully Automatic Liver Segmentation through Graph-Cut Technique," in *Conf Proc IEEE Eng Med Biol Soc*, 2007, pp. 5243-5246.

[7] L. Grady, "Random walks for image segmentation," *IEEE Trans. Pattern Anal. Mach. Intell.,* vol. 28, pp. 1768-1783, 2006.

[8] J. Zhang, J. W. Modestino, *et al.*, "Maximum-likelihood parameter estimation for unsupervised stochastic model-based image segmentation," *IEEE Trans. Image Process.,* vol. 3, pp. 404-420, 1994.

[9] R. H. Davies, C. J. Twining, *et al.*, "Building 3-D Statistical Shape Models by Direct Optimization," *IEEE Trans. Med. Imaging,* vol. 29, pp. 961-981, 2010.

[10] K. Van Leemput, "Encoding Probabilistic Brain Atlases Using Bayesian Inference," *IEEE Trans. Med. Imaging,* vol. 28, pp. 822-837, 2009.

[11] V. Caselles, R. Kimmel, *et al.*, "Geodesic active contours," *Int. J. Comput. Vis.,* vol. 22, pp. 61-79, 1997.

[12] A. Wimmer, G. Soza, *et al.*, "A Generic Probabilistic Active Shape Model for Organ Segmentation," in *Proc. of Med. Image. Comput. Comput. Assist. Interv.*, 2009, pp. 26-33.

[13] Y. Y. Boykov and M. P. Jolly, "Interactive graph cuts for optimal boundary & region segmentation of objects in N-D images," in *Proc IEEE Comput. Soc. Conf. Comput. Vis. Pattern Recognit.*, 2001, pp. 105-112 vol.1.

[14] B. Xue and G. Sapiro, "A Geodesic Framework for Fast Interactive Image and Video Segmentation and Matting," in *Proc. IEEE Int'l Conf. Computer Vision*, 2007, pp. 1-8.

[15] Y. Wenxian, C. Jianfei, *et al.*, "User-Friendly Interactive Image Segmentation Through Unified Combinatorial User Inputs," *IEEE Trans. Image Process.,* vol. 19, pp. 2470-2479, 2010.

[16] R. P. Browne, P. D. McNicholas, *et al.*, "Model-Based Learning Using a Mixture of Mixtures of Gaussian and Uniform Distributions," *IEEE Trans. Pattern Anal. Mach. Intell.,* vol. 34, pp. 814-817, 2012.

[17] L. Grady, "Multilabel random walker image segmentation using prior models," in *Proc. IEEE Conf. Computer Vision and Pattern Recognition*, 2005, pp. 763-770 vol. 1.

[18] L. Soler, A. Hostettler, *et al.* 3D Image Reconstruction for Comparison of Algorithm Database : A patient-specific anatomical and medical image database [Online]. Available: http://www.ircad.fr/softwares/3Dircadb/3Dircadb.php?lng=en

[19] A. Blake, C. Rother, *et al.*, "Interactive image segmentation using an adaptive GMMRF model," in *Proc. European Conf. Computer Vision*, 2004, pp. 428-441.

[20] C. Couprie, L. Grady, *et al.*, "Power watershed: a unifying graph-based optimization framework," *IEEE Trans. Pattern Anal. Mach. Intell.,* vol. 33, pp. 1384-1399, 2011.